ELSEVIER

Contents lists available at ScienceDirect

Applied Surface Science

journal homepage: www.elsevier.com/locate/apsusc



Full Length Article

Structural damage and phase stability of cobalt-free FeCrNi medium-entropy alloy under high-fluence ion irradiation

Ao Fu^a, Bin Liu^{a,*}, Fusheng Tan^b, Yuankui Cao^a, Jia Li^{b,*}, Bo Liu^c, Qihong Fang^b, Peter K. Liaw^d, Yong Liu^a

- ^a State Key Laboratory of Powder Metallurgy, Central South University, Changsha 410083, China
- b State Key Laboratory of Advanced Design and Manufacturing for Vehicle Body, College of Mechanical and Vehicle Engineering, Hunan University, Changsha 410082, China
- ^c Key Laboratory of Radiation Physics and Technology of Ministry of Education, Institute of Nuclear Science and Technology, Sichuan University, Chengdu 610064, China
- Department of Materials Science and Engineering, The University of Tennessee, Knoxyille, TN 37996, USA

ARTICLE INFO

Keywords: Medium-entropy alloy Microstructure Powder metallurgy Ion irradiation Radiation damage Molecular dynamics simulation

ABSTRACT

A cobalt-free FeCrNi MEA was successfully synthesized and irradiated with 7.5 MeV Au ions at room temperature over a wide fluence from 5×10^{15} to 5×10^{16} Au ions/cm². Microstructural characterization shows that the FeCrNi MEA exhibits low structural damage and high phase stability under high-fluence ion irradiation, and diffuse dislocations and defect clusters, especially dislocation loops and stacking-faults (SFs), are the main microstructural feature after irradiation. Limited elemental segregation at grain-boundaries and nanoscale Au clusters can be observed only in the specimen irradiated at the highest fluence. Meanwhile, void formation and phase instability are absent in any irradiation condition. Cascade-collision simulation reveals that large-size vacancy cluster collapses into the stacking fault tetrahedrons (SFTs) and abundant dislocation structures, especially the high-fraction movable Shockley dislocations at the high-energy ion irradiation, contributing to the absence of voids and the easily activated dislocation networks. Owing to these microstructural features, the irradiated specimens only exhibit a slight hardness increase (26 % at 210 dpa), indicating a superior resistance to irradiation hardening. Overall, this work supports that the FeCrNi MEA possesses an outstanding irradiation tolerance especially under high-fluence ion irradiation, thereby having good application prospects in the field of advanced nuclear reactors.

1. Introduction

As the global energy demands are increasing at an unprecedented rate, advanced nuclear energy systems with higher safety, less pollution, and stronger competitiveness, especially the fourth-generation fission or fusion reactors [1–3], have attracted extensive attention all over the word. Structural materials used in the advanced nuclear energy systems require extraordinary performance due to the extremely harsh service environments, such as the higher operating temperature, larger radiation dose, stronger corrosive of heat transfer medium, and longer working life [3,4]. Continuous high-energy ions radiation will cause serious material damage, including void swelling, hollow, elemental segregation, and phase instability, and lead to the degradation of mechanical properties [5–8], which will seriously affect the safety and

reliability of the reactors. Although large efforts have been made over the past half century, the material degradation in harsh environments cannot be completely overcome.

Recently, a new type of multi-principal element (MPE) alloy system, also named as medium/high-entropy alloys (M/HEAs) [9–13], has been proposed, opening the door to design and develop materials by changing the type and concentration of each component. The M/HEAs break through the traditional alloy design concepts based on one or two principal elements, and are composed of multiple principal elements with equal or near-equal atomic ratios. Due to their high mixing entropy, the M/HEAs are easy to form simple-phase structures (e.g., face-centered cubic, fcc, or body-centered cubic, bcc) without harmful secondary phases [14–17]. The unique microstructures of the M/HEAs lead to their promising properties, such as high strength, excellent ductility,

E-mail addresses: binliu@csu.edu.cn (B. Liu), lijia123@hnu.edu.cn (J. Li).

^{*} Corresponding authors.

outstanding corrosion resistance, and good phase stability. Moreover, a series of recent works on the M/HEAs shows that this alloy system may have higher irradiation resistance than traditional structural alloys (i.e., Fe-Cr-Ni series austenite stainless steels (SSs)) [8,11,17], such as the enhanced swelling resistance, suppressed elemental segregation, reduced damage accumulation, and so on, making them potential candidates for high-performance nuclear energy materials. However, most of the M/HEAs studied so far incorporate cobalt, such as FeCoCrNiMn, FeCoCrNi, CoCrNi, etc., which has highly induced radioactivity when exposed to neutrons irradiation [18–20], and are not suitable for nuclear energy applications.

In this work, a cobalt-free FeCrNi MEA with a balanced tensile strength and ductility combination (1035 MPa, 54 % [10]) was successfully fabricated via hot extrusion, and then irradiated at room temperature over a wide Au ions fluences. This study provides systematical experimental investigations on the microstructural evolution (i.e., structural damage and phase stability) and hardening behavior of the FeCrNi MEA under high-fluence ion irradiation, and attempts to understand the irradiation-damage mechanism from an atomic-scale perspective by molecular dynamic (MD) simulation.

2. Experiments and simulations

2.1. Experimental procedures

The FeCrNi MEA was fabricated by hot extrusion of high-purity (99.99 %) spherical FeCrNi gas-atomized powders, and the extrusion temperature and ratio of 1150 °C and 7:1, respectively [10]. Specimens (Φ 10 mm \times 3 mm) for ions irradiation were cut from the extruded bar along the extrusion direction, and the chemical composition was determined to be Fe_{33.7}Cr_{33.7}Ni_{32.5} (atomic percent, at.%). Their surfaces were firstly ground to 2000 grit by using SiC paper, and finally polished by diamond paste. After that, the polished specimens were divided into three groups, and irradiated with 7.5 MeV Au ions at three different fluences of 5×10^{15} ions/cm², 1×10^{16} ions/cm², and 5×10^{16} ions/cm², respectively, at room temperature. The irradiation tests were performed on the implantation system at the Southwest Institute of Physics of China. The data of damage level in displacements per atom (dpa), Au ions concentration, and damage depth were calculated by SRIM 2008 (40 eV displacement threshold energy for all the constituent elements). Fig. 1 shows the curves of three groups of specimens irradiated at three different Au ions fluences, exhibiting similar Au-ions

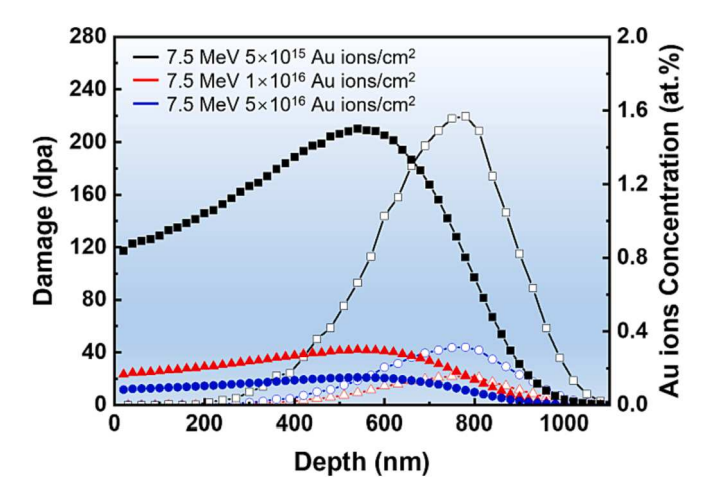


Fig. 1. SRIM simulations showing the damage (left solid line) and implanted ion profiles (right dashed line) of the FeCrNi MEA irradiated with 7.5 MeV Au ions at room temperature over a wide fluence from 5×10^{15} ions/cm² to 5×10^{16} ions/cm². Notice that the square, round, and triangle represent the irradiation fluences of 5×10^{15} ions/cm², 1×10^{16} ions/cm², and 1×10^{16} ions/cm², respectively.

distributions and damage distributions, and the maximum damage fluences reach 21 dpa, 42 dpa, and 210 dpa, respectively. In order to investigate the irradiation-induced microstructural evaluation, the specimen irradiated at the highest fluence of 5×10^{16} Au ions/cm 2 was systematically characterized.

Chemical composition was determined by an inductively coupled plasma mass spectrometry (ICP-MS) analysis. Phase characterization was performed by a grazing incidence X-ray diffractometer (GiXRD, Advance D8). Microstructure was investigated by a scanning electron microscope (SEM, Helios Nanolab 600i) equipped with energy dispersive X-ray spectroscopic (EDS) device, electron backscatter diffraction (EBSD), and focused ion beam (FIB) instruments. Specimens for transmission electron microscope (TEM) observation were cut by the FIB instrument along the irradiation direction. The detailed microstructure was analyzed by a Tecnai G2 TF30 operating at 300 kV. Nanoindentation tests of the unirradiated and irradiated specimens were performed on an IBIS nano-indenter. The continuous stiffness measurement (CSM) technique in an XP mode was chosen to determine hardness versus depth curves. To ensure accuracy, each specimen was tested at least 3 times, and the results are averaged for analysis. The Nix and Gao method [7,21] is employed to calculate the hardness of the unirradiated and irradiated specimens, and the relationship between the hardness and indentation depth can be described by the following equation: $H^2 = H_0^2(1 + h^*/h)$, where H is the hardness at the indentation depth, H_0 is the hardness at the infinite depth, and h^* is a characteristic length.

2.2. Molecular dynamic simulations

To reveal the details of the microstructure evolution in the FeCrNi MEA under high-energy ion irradiation, the cascade collision is simulated by the MD method. The MD simulations are carried out, based on the Large-scale Atomic/Molecular Massively Parallel Simulator (LAMMPS) [22]. The OVITO software is used for visualization [23]. The atomic model of the equimolar FeCrNi single crystal is constructed by the general technique [24,25]. A pure Ni single crystal with an fcc structure is first built, then the elements of atoms are randomly replaced until the desired composition fraction is reached. The crystal orientations along X, Y and Z directions are [100], [010], and [001], respectively. A cubic simulation box is used to simulate the cascade collision in FeCrNi single crystal. The dimensions of the simulation box are (X, Y, Z) = (195.25 Å, 195.25 Å, 195.25 Å), which are large enough to simulate the cascade collision using MD simulations [Crack-healing mechanisms in high-entropy alloys under ion irradiation; The effect of grain boundary on irradiation resistance of CoCrCuFeNi high entropy alloy; The interactions between dislocations and displacement cascades in FeCoCrNi concentrated solid-solution alloy and pure Ni].

After constructing the initial model of the FeCrNi single crystal, the structure of the initial model is optimized by the molecular static simulation with a conjugate gradient algorithm. Then the model is relaxed under an isothermal-isobaric (NPT) ensemble for 100 ps, during which the temperature is fixed at 300 K, and the pressures along the X/ Y/Z directions are 0 bar. For all above procedures, the periodic boundary condition is applied for all directions, and the time step is fixed at 0.001 ps. To simulate the cascade collision, we designate an Ni atom within the FeCrNi MEA model as the primary knock-on atom (PKA), as described in previous studies [Crack-healing mechanisms in high-entropy alloys under ion irradiation; Interactions between displacement cascades and grain boundaries in NiFe single-phase concentrated solid solution alloys]. The initial velocity of the PKA is determined based on the desired kinetic energy. It is essential to highlight that the PKA can alternatively be an Fe or Cr atom, and the outcomes are independent of the specific element chosen for the PKA. It is worth noting that when selecting different atoms as the PKA, adjustments to the initial velocity should be made according to their atomic mass. This ensures consistency in achieving the targeted initial kinetic energy for the PKA. In this work, the PKA energies of 10 KeV and 40 KeV are used to simulate the low-energy and high-energy collision cascades. The initial velocity direction of the PKA is the negative Z-axis direction. The cascade collision is performed under the microcanonical ensemble (NVE). Two boundary layers (10 Å thickness) at the Z direction are set as a thermostatic layer with a constant temperature of 300 K. The time step varies in the range of [0.00001 fs, 0.5 fs] to ensure that the displacement of atoms per time step does not exceed 0.005 times the lattice constant. For all simulations, the atomic interaction is descripted using the embedded-atom method (EAM) FeNiCr potential created by Béland [26]. This potential is updated to handle the short-range interactions based on an ab-initio based framework. The equilibrium lattice parameter of the equimolar FeCrNi MEA predicted by the EAM potential is 3.55 Å, which is close to the experimental data shown in later phase analysis. Using this potential, the primary damage production of the Ni-Fe-Cr system during collision cascades can be well predicted [26].

3. Results and discussion

3.1. Initial microstructure

Fig. 2a shows the EDS maps of the extruded FeCrNi MEA, confirming the homogeneous distribution of elements, Fe, Cr, and Ni. It is noteworthy that no secondary phases or elemental segregation can be observed. The typical inverse pole figure (IPF) map (Fig. 2b) shows that the FeCrNi MEA consists of equiaxed grains with a grain size of $\sim\!12~\mu m$. Numerous annealing twins appear within the grains, indicating a low stacking fault energy (SFE) of the FeCrNi MEA [27,28].

3.2. Phase analysis

Fig. 3a shows the GIXRD patterns of the unirradiated and irradiated specimens at three different fluences of 5×10^{15} Au ions/cm², 1×10^{16} Au ions/cm², and 5×10^{16} Au ions/cm², respectively. It can be clearly seen that all the specimens consist of single-phase fcc structure, and no detectable diffraction peaks of a secondary phase appear, indicating that the FeCrNi MEA exhibits extraordinary phase stability even irradiated at a high fluence of ~210 dpa. After Au-ions irradiation, the broadening of diffraction peaks can be observed, which is mainly due to the formation of irradiation-induced defects [6,7]. Interestingly, the diffraction peaks slightly shift to a lower Bragg angle with the increased irradiation fluence, meaning a slight lattice expansion. The related lattice parameters increase from the initial 3.5977 Å to 3.6211 Å (Fig. 3b). The lattice

expansion can be attributed to the implantation of heavy Au ions [6].

3.3. Irradiation microstructure

Fig. 4 shows the microstructure along the irradiation direction for the specimen irradiated at the lowest fluence of 5×10^{15} Au ions/cm². For a better comparison, the damage fluence and Au ions concentration as a function of depth from the surface are presented in Fig. 4a. The peaks of damage fluence of ~21 dpa and Au ions concentration of ~0.16 at.% appear at a depth of ~540 nm and ~780 nm, respectively, below the surface. Fig. 4b and 4c show the elected area electron diffraction (SAED) pattens and microstructure in the high-damage region. It can be seen that the diffraction spots are very sharp, and there is no obvious amorphization phenomenon. As shown in Fig. 4c, a high density of small defect clusters forms in the high-damage region over the depth range from 400 nm to 700 nm. To investigate the irradiation-induced segregation behavior, EDS line scanning was performed across the grain boundary in the high-damage region as shown in Fig. 4d. Obviously, the elements of Fe, Cr, and Ni are uniformly distributed, and no elemental segregation can be found.

Fig. 5 shows the microstructure of the specimen irradiated at the highest fluence of 5×10^{16} Au ions/cm². As shown in the damage fluence and Au-ions concentration distribution curves, it can be found that the peaks of damage fluence of ~210 dpa and Au ions concentration of \sim 1.57 at.% appear at a depth of \sim 540 nm and \sim 780 nm, respectively. The elemental distribution map in Fig. 5b also shows the variation of Auions concentration with the implantation depth from the surface. Consistent with the SRIM simulation result, the Au ions are mainly concentrated in a narrow region with a depth between ~550 nm and \sim 1050 nm. The SAED patterns along the z=[011] axis at different irradiation depths from the surface shown in Fig. 5c also reveal that the FeCrNi MEA maintains a single-phase fcc structure after irradiation even at a high damage fluence (~210 dpa). No diffraction rings corresponding to amorphous structures appear in these SAED patterns, showing that the FeCrNi MEA exhibits good amorphization resistance. The HEA/ MEA generally exhibit excellent resistance to high-energy ions irradiation. Sadeghilaridjani et al. [8] found that the HfTaTiVZr HEA has good phase stability and amorphization resistance after the 4.4 MeV Ni ions irradiation up to 30 dpa at room temperature. Xia et al. [2,29] reported that the Al_xCoCrFeNi HEA exhibits excellent phase stability, and no significant elemental segregation, secondary phase, or amorphous structures can be detected under 3 MeV Au ions irradiation at room temperature up to 105 dpa. In contrast, most of the traditional alloys, such as steels, refractory alloys, and intermetallics, are prone to

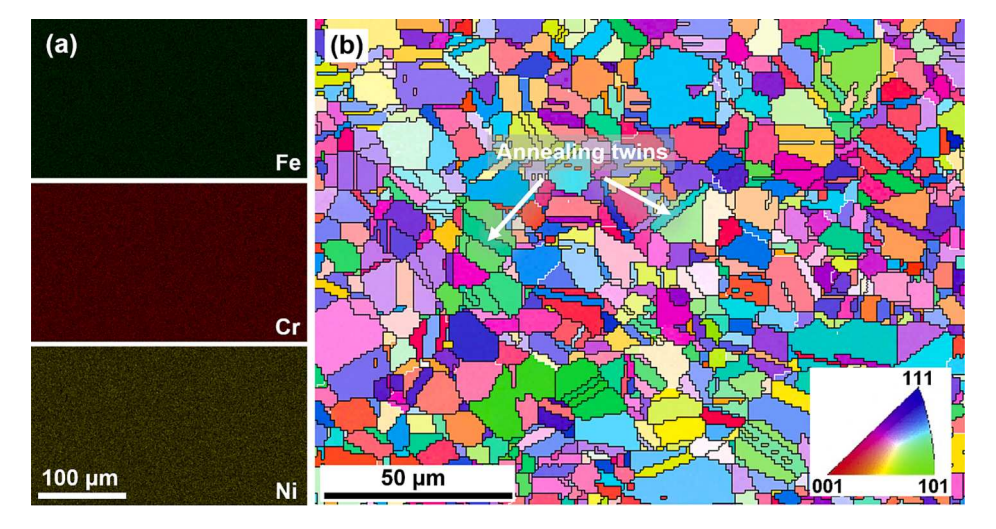


Fig. 2. (a) EDS maps showing the homogeneous distribution of elements, Fe, Cr, and Ni in the FeCrNi MEA; (b) IPF map presenting the equiaxed grains and annealing twins.

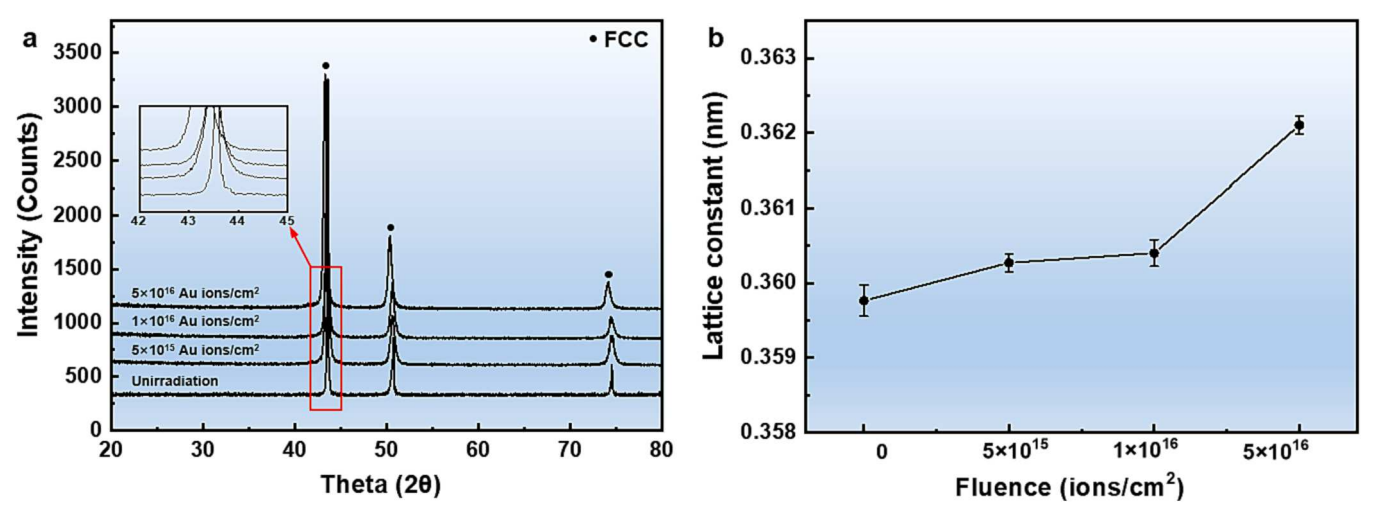


Fig. 3. (a) GIXRD patterns of the unirradiated and irradiated FeCrNi MEA at three different fluences of 5×10^{15} Au ions/cm², 1×10^{16} Au ions/cm², and 5×10^{16} Au ions/cm², respectively; (b) the lattice parameter as a function of the irradiation fluence.

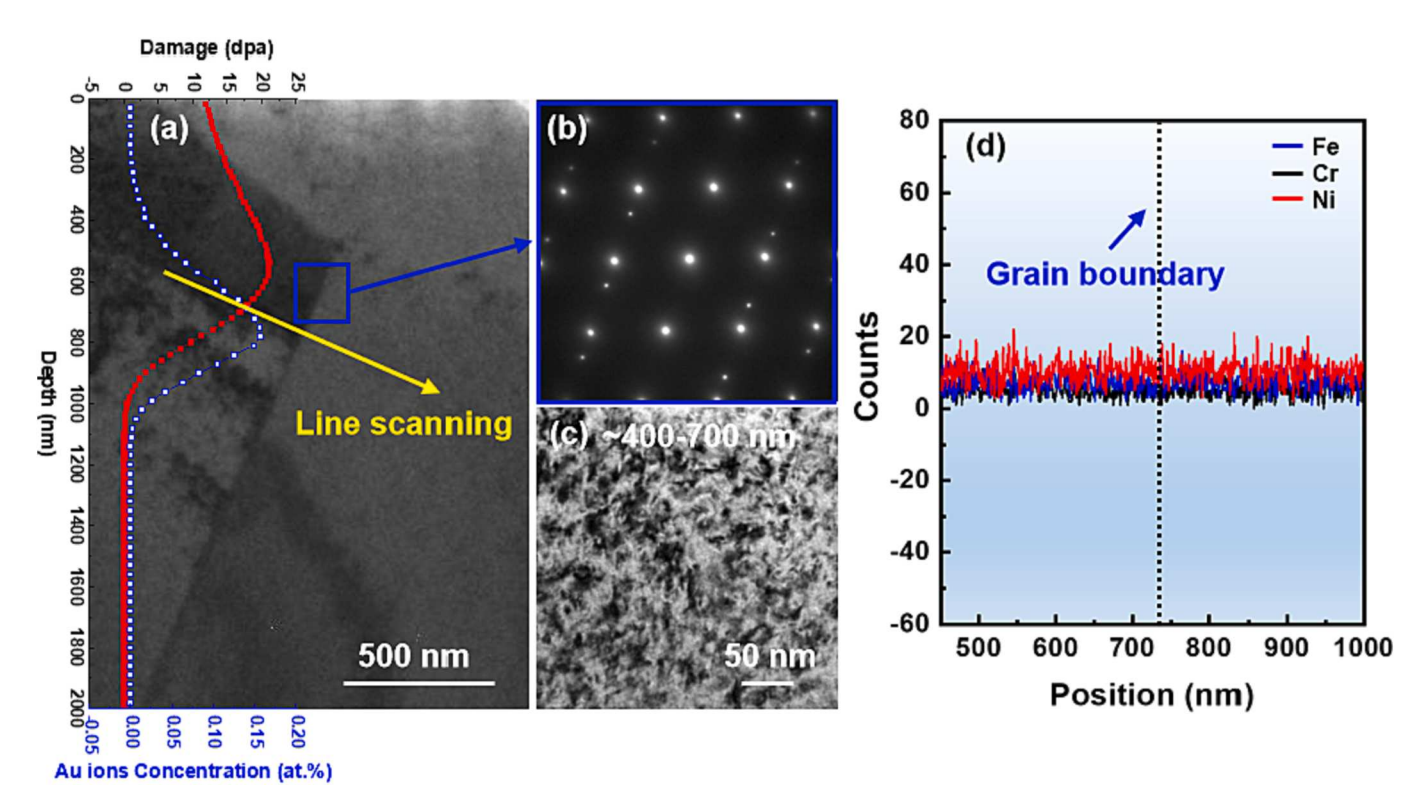


Fig. 4. (a) Bright-field (BF) TEM images showing the microstructure of the FeCrNi MEA irradiated at the lowest fluence of 5×10^{15} Au ions/cm²; (b) SAED patterns presenting a single-phase fcc structure; (c) BF TEM image showing a high density of small defect clusters; (d) EDS line scanning exhibiting the elemental distribution across the grain boundary.

amorphization at a low irradiation fluence and show a significantly higher damage level [8]. Superior irradiation structural stability of the M/HEAs can be attributed to the severe lattice distortion and sluggish diffusion, leading to slower defect mobility and stronger self-healing ability [8,30].

Fig. 6 presents TEM images of the specimens irradiated at the highest fluence of 5×10^{16} Au ions/cm². The size and density of irradiation-induced defects vary with the depth from the surface. According to the size and density of the defects, the microstructure, as shown in Fig. 6a, can be divided into two completely different regions, low damage region and high damage region. In the low damage region with a depth lower than 350 nm, only low density of dislocations and black

dots can be found as presented in Fig. 6a and 6b. Most of the small defect clusters, such as interstitial loops or stacking-fault tetrahedras (SFT), appear as black dots smaller than ~ 5 nm in the irradiated M/HEAs [5]. However, the density of dislocations and defect clusters significantly increases with the depth, and the high-damage region with a depth exceeding 350 nm contains a high density of dislocations and defect clusters. The details of microstructures in the high-damage region are displayed in Fig. 6c-6f. Obviously, the irradiation-induced dislocation loops (Fig. 6c) and stacking faults (SFs) (Fig. 6d) are considered as the primary defects in this region. *Yang et al.* [31] also found dislocations, dislocation loops, and SFTs when they investigated the single-phase fcc $Al_{0.1}$ CoCrFeNi HEA in the high-damage region (~ 31 dpa) after 3 MeV-

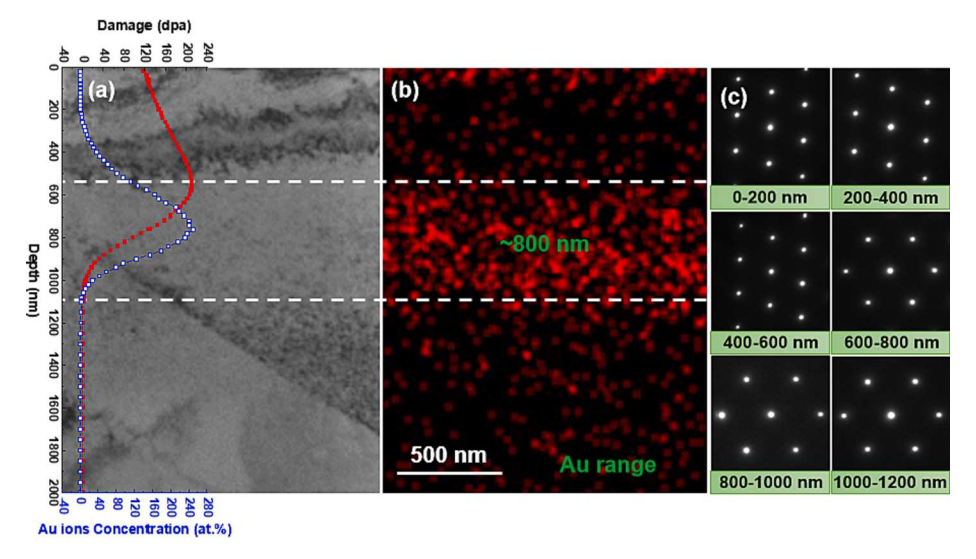


Fig. 5. (a) BF TEM images showing the microstructure of the FeCrNi MEA irradiated at the highest fluence of 5×10^{16} Au ions/cm²; (b) elemental-distribution map presenting the variation of Au-ions concentration with the depth from the surface; (c) SAED patterns at different depths below the surface showing a single-phase fcc structure.

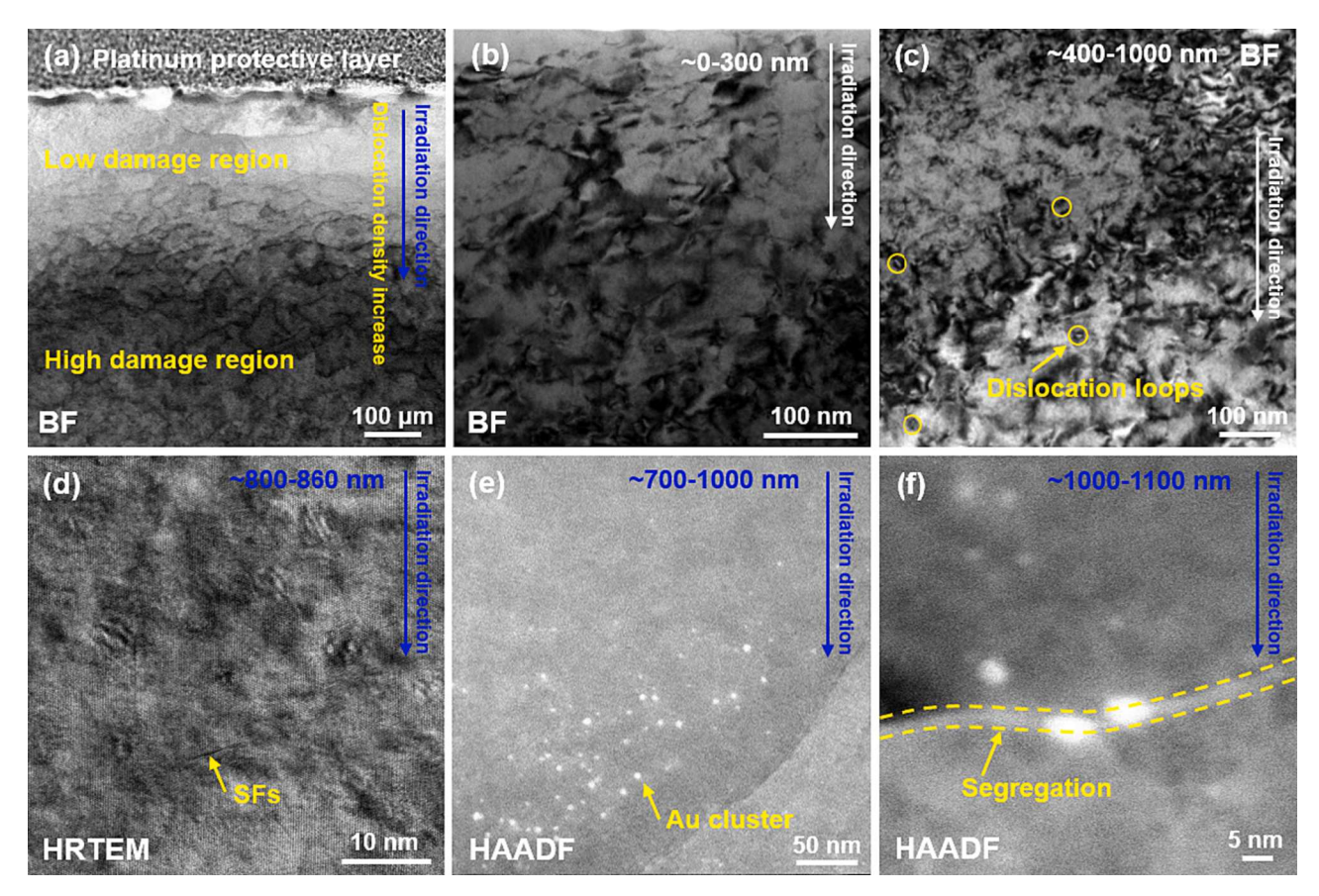


Fig. 6. Microstructural characterizations of the FeCrNi MEA irradiated at the highest fluence of 5×10^{16} Au ions/cm². BF images showing (a) the dislocation distribution, (b) the dislocations and defect clusters, (c) the dislocation loops; high-resolution TEM (HRTEM) image showing (d) the SFs; high-angle annular dark-field detector (HAADF) images presenting (e) the Au clusters and (f) the elemental segregation.

Au ions irradiation.

The irradiation-induced white dots, as shown in HAADF image (Fig. 6e), are another interesting phenomenon in the specimen irradiated at highest fluence, and they mainly appear in a narrow region with a depth from $\sim\!\!700$ nm to $\sim\!\!1100$ nm. These white dots are very dispersive and fine with an average diameter of $\sim\!\!5$ nm. The detailed

elemental maps (Fig. 7) confirm that these dispersed white dots are enriched with Au and indeed Au clusters. At the same time, Ni is slightly segregated at Au clusters, but Fe and Cr show an opposite distribution tendency. However, the Au clusters can only form in the high-damage region of the specimens irradiated at the highest fluence of 5×10^{16} Au ions/cm², and no Au clusters can be observed in the specimens

Fig. 7. HAADF images and elemental distribution maps showing the dispersed Au clusters.

irradiated at low Au fluences. This irradiation-induced white dots are also absent in the $\rm Al_{0.1}CoCrFeNi$ HEA (~31 dpa) [31], $\rm Al_{0.3}CoCrFeNi$ MEA (~31 dpa) [5], $\rm Al_{x}CoCrFeNi$ MEA (~105 dpa) [2], and FeCoCrNi HEA (~49 dpa) [32] with Au-ions irradiation at moderate damage fluences. For example, the Au ions are uniformly distributed in the Al_x-CoCrFeNi MEA after Au-ion irradiation [5,31]. Moreover, it is worth mentioning that irradiation-induced elemental segregation occurs at grain boundaries in the high-damage region (Fig. 6f), which will be investigated in detail later.

Fig. 8a shows the depth distribution of the Au clusters in the FeCrNi MEA at the highest irradiation fluence of 5×10^{16} Au ions/cm², and the related data is statistically analyzed from the TEM images. Apparently, the Au clusters are mainly distributed in a depth from ~750 nm to ~1050 nm, and the trend of the depth distribution of Au clusters is consistent with the SRIM-simulation results (the peak density of the Auions concentration is located at a depth ~800 nm, as shown in Fig. 5b), but the peak position is slightly deeper. This small deviation in the peak position can be attributed to the following reasons. Firstly, the materials used for SRIM simulation are traditional solid solutions, while the M/ HEAs have a specific rock-salt structure with high lattice distortion [7]. Secondly, the statistical deviation may also affect the comparison results. The defects and defect clusters induced by heavy-ions irradiation are more concentrated than those induced by lighter-ions irradiation [17]. The morphology of Au clusters in the region at a depth from \sim 750 nm to ~1050 nm is very clear and easy to count. However, the Auclusters density in a depth below ~750 nm and above ~1050 nm is very low, and their size is small, which will lead to a low statistical number of Au clusters. The size distribution of the Au clusters is clearly shown in Fig. 8b. The Au clusters have a tiny size with an average diameter of 3.5 nm. By comparing with traditional alloys, the M/HEAs usually exhibit a superior irradiation resistance, and the irradiationinduced defect cluster size is often smaller. The compositional complexity and unique microstructures of the M/HEAs may explain the improved irradiation resistance [2,17]. The high compositional complexity in the M/HEAs can induce the strong lattice distortion and lower the defect formation/migration mobility, which can play an

important role in suppressing the coalescence and growth of defect clusters and result in smaller defect-cluster sizes [2,7]. At the same time, the reduced thermal conductivity of the M/HEAs may promote their "self-healing" effect, which can also hinder the defect movement and growth and lead to smaller damage defects [2]. Furthermore, the number of equilibrium vacancy defects in the M/HEAs is significantly larger than that in pure metals or traditional binary alloys, and these dispersed vacancy defects can effectively capture the implanted ions and disperse the ions agglomeration, thereby retarding the growth of irradiation-induced defect clusters [33,34].

Fig. 9 shows the HAADF images of grain boundaries located at different irradiation regions with a depth of 300 nm, 500 nm, 900 nm, 1000 nm, respectively, and the related elemental distribution of Fe, Cr, Ni, and Au. Random grain boundaries are selected for investigating the elemental distribution. According to the elemental-distribution maps, there is undetectable segregation along the grain boundaries in the regions, A and B, respectively, indicating that the FeCrNi MEA still maintains good radiation-induced segregation resistance in these regions. While the elemental segregation can be observed in the regions, C and D, with a depth of \sim 900 nm and \sim 1000 nm, respectively, which are the regions with high damage fluences. As shown in Fig. 9c and 9d, Ni segregates at the grain boundaries, while Fe and Cr are depleted near the grain boundaries. Similar segregation behavior has been observed in many irradiated Fe-Cr-Ni materials, such as FeCoCrNiMn HEA [35], FeCoCrNi HEA [36], FeCrMnNi HEA [30], Al_{0.1}CoCrFeNi HEA [29], and Fe-Cr-Ni SSs [37,38]. Generally, the reverse Kirkendall mechanism can be used to explain the segregation behavior of the major elements (i.e., Fe, Cr, and Ni) at the grain boundaries in the Fe-Cr-Ni materials [30,39]. The segregation behavior significantly depends on the solute mobility, and the defect sinks (i.e., dislocations, detects, defect clusters, and grain boundaries) are usually enriched with undersized solutes (high mobility) but depleted in oversized solutes (low mobility), and the atom radii for Fe, Co, Cr, and Ni are 1.56 Å, 1.52 Å, 1.66 Å, and 1.49 Å, respectively. For example, the undersized solutes, Co and Ni, enriched and the oversized solutes, Fe and Cr, depleted at the dislocations and dislocation loops can be found in the Au-ions-irradiated Al_{0.1}CoCrFeNi

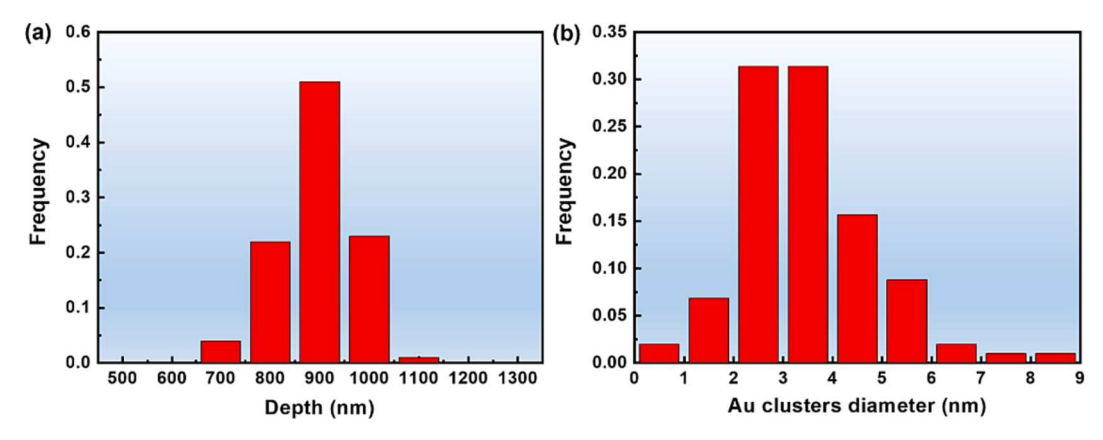


Fig. 8. (a) The depth distribution and (b) the size distribution of the Au clusters in the FeCrNi MEA irradiated at the highest fluence of 5×10^{16} Au ions/cm².

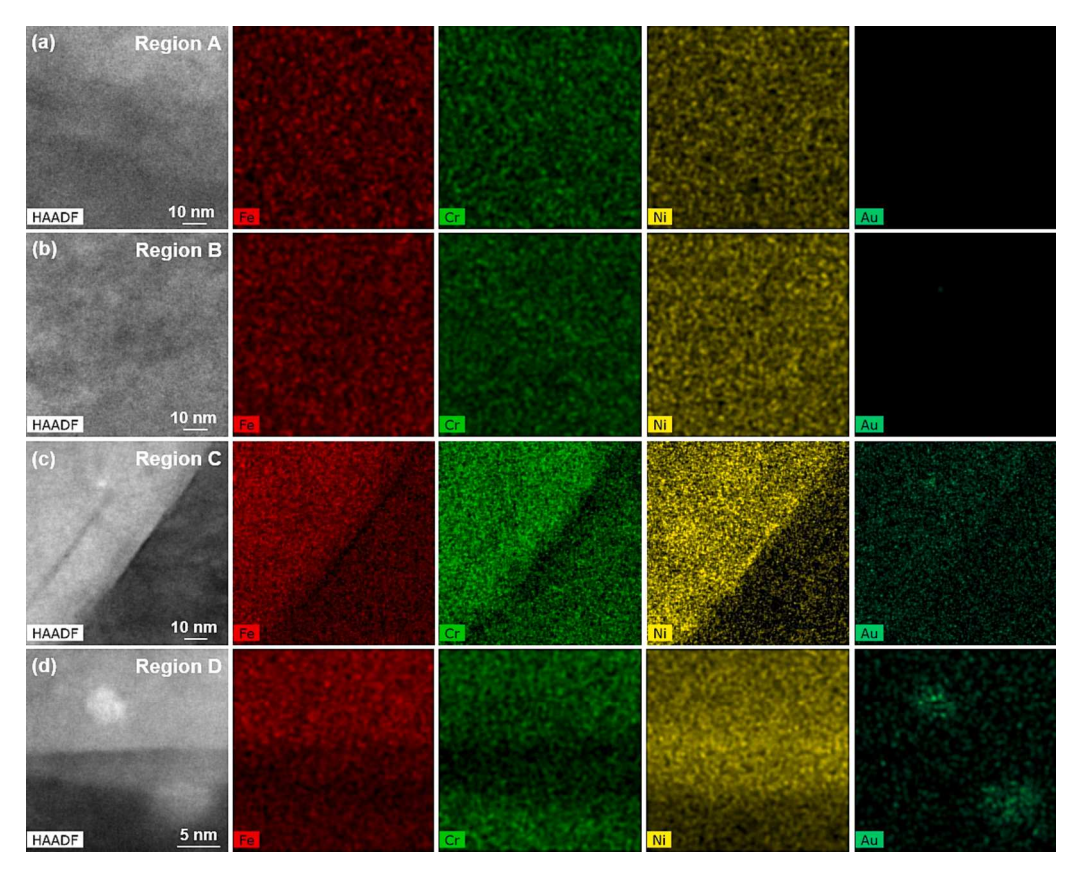


Fig. 9. HAADF images and elemental maps showing the irradiation-induced segregation at grain boundaries in different regions with incremental depths of (a) 300 nm, (b) 500 nm, (c) 900 nm and (d) 1000 nm, respectively.

HEA [31]. Therefore, for the FeCrNi HEA, the grain boundaries in the high-damage region will be enriched with the faster diffuser, Ni, but depleted in the slower diffusers, Fe and Cr. However, it is worth noticing that the FeCrNi MEA irradiated at a low fluence of 5×10^{15} Au ions/cm² (Fig. 4d) does not have any detectable elemental segregation, exhibiting good irradiation-induced segregation resistance. *Kumar et al.* [30] also found that the M/HEAs have relatively low solute diffusivity when comparing the radiation-induced elemental segregation of the FeNiMnCr HEA and traditional Fe-Cr-Ni SSs. This trend mainly results from the fact that the lattice potential sites of the M/HEAs fluctuate dramatically, which leads to the existence of a large number of low-energy lattice-potential sites, thereby reducing the diffusion kinetic of solute atoms.

Moreover, no detectable voids are found in the FeCrNi MEA at the highest irradiation fluence of 5×10^{16} Au ions/cm², indicating that the FeCrNi MEA exhibits outstanding irradiation-induced void swelling resistance. Lu et al. [40] compared the void-swelling resistance of different materials, including the nickel, NiCo alloy, NiFe alloy, NiCoFe MEA, NiCoFeCr HEA, and NiCoFeCrMn HEA under Ni-ions irradiation, and found that only small voids can be observed in the NiCoFe MEA, NiCoFeCr HEA, and NiCoFeCrMn HEA, but larger voids appear in the nickel, NiCo alloy, and NiFe alloy irradiated in the same condition. Tuomisto et al. [41] investigated the microstructural evolution of the FeCoCrNi HEA and Fe-Cr-Ni SS irradiated by Ni ions at damage fluences ranging from 0.03 dpa to 10 dpa and found that the FeCoCrNi HEA exhibits superior resistance to void swelling. Tunes et al. [42] studied the void-formation behavior of the FeCrMnNi HEA and AISI-348 SS after light and heavy ions irradiation under the same damage fluence, and the results show that the size and distribution of voids in the irradiated-FeCrMnNi HEA are effectively restricted, compared to the AISI-348 SS. Due to the unique microstructures of the M/HEAs, the movement of defect clusters in the alloys will change from a long-range onedimensional mode to a short-range three-dimensional mode during the irradiation process, which can effectively inhibit the formation and growth of the irradiation-induced voids [40]. This is the main reason for the improved void-swelling resistance.

3.4. Hardness

Since the irradiation depth is usually limited to a few micrometers from the surface, nanoindentation tests are considered as an effective way to characterize the irradiation induced mechanical behavior. Fig. 10a shows the hardness as a function of indentation depth below 750 nm of the unirradiated and irradiated specimens at three different Au- ions fluences. Owing to the effects of the reverse indentation-size effect and specimens-surface uncertainty, the hardness data corresponding to a depth below 150 nm should be ignored. It can be observed that the hardness for the unirradiated and irradiated specimens decreases with increasing the indentation depth, and the FeCrNi MEA shows an irradiation-hardening phenomenon in the entire depth range with the increase of irradiation fluences.

The variation of H^2 as a function of the 1/h for the FeCrNi MEA before and after irradiation is plotted in Fig. 10b, which is used to determine the real hardness. For the unirradiated specimen and low-fluence irradiated specimens, there is a good linearity between H^2 and 1/h when the indentation depth is greater than 150 nm. However, for the moderate/high-fluence-irradiated specimens, the fitted curves have evident inflection points at a depth of \sim 300 nm, and all the curves exhibit bilinearity. The calculated real hardness of the unirradiated and irradiated FeCrNi MEA are 3.2 GPa, 3.27 GPa, 3.79 GPa, and 4.02 GPa, respectively. It can be found that the hardness of the specimens slightly increases with the increased irradiation fluences. For example, the hardness increased by 26 % at the highest irradiation fluence. Similar irradiation hardening was also observed in some other M/HEAs (e.g.,

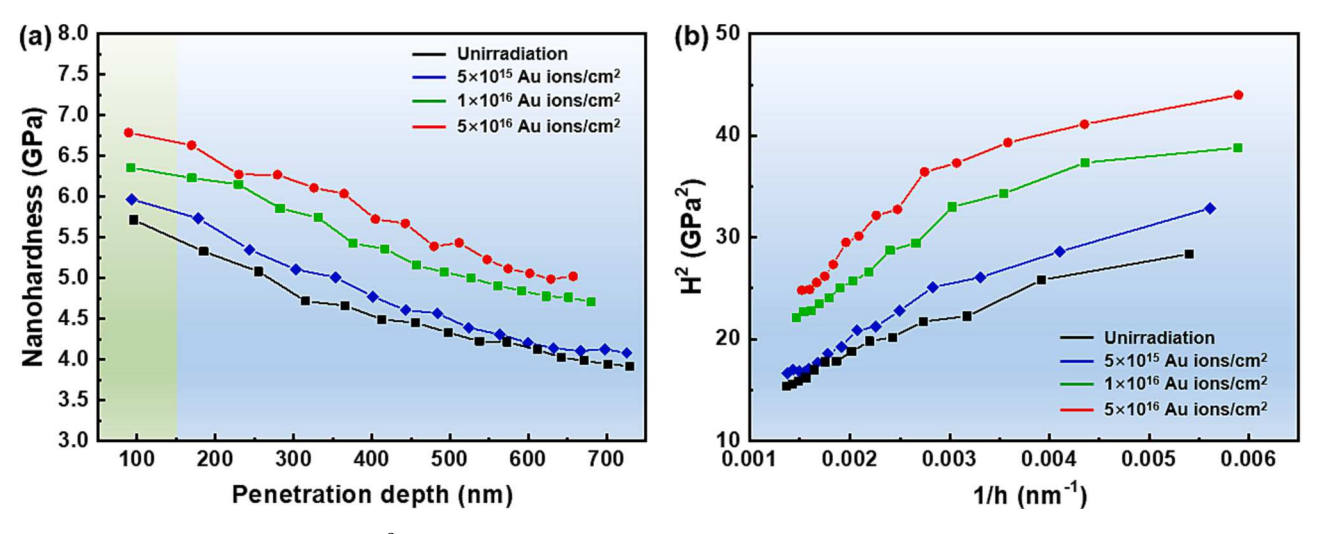


Fig. 10. (a) Nanoindentation hardness and (b) H^2 versus the indentation depth of the FeCrNi MEA before and after irradiation with 7.5 MeV Au ions over a wide fluence from 5×10^{15} ions/cm² to 5×10^{16} ions/cm².

FeNiMnCr [30], $Fe_{38}Mn_{40}Ni_{11}Al_4Cr_7$ [43], HfTaTiVZr Ti₂ZrHfV_{0.5}Mo_{0.2} [33]) and other traditional materials, such as SSs [8], but the irradiated hardening in the M/HEAs is much slighter than that in the traditional materials. Sadeghilaridjani et al. [8] reported that the irradiation hardening is \sim 13 % for the HfTaTiVZr HEA while \sim 50 % for the 304 SS under the same irradiation condition. The irradiation hardening is mainly due to the formation of the irradiation-induced obstacles, such as dislocations, defects, and defect clusters, including dislocation loops and SFs, which can hinder the dislocation motion on the slip plane [7,8]. However, compared with traditional materials, the defects in the M/HEAs have higher formation energy and atomic-level stress [8], which will cause the defects to be unstable and easy to annihilate. Therefore, the irradiated M/HEAs have a significantly lower defect density, resulting in reduced irradiation-induced hardening.

3.5. Atomic-scale insights into the irradiation-damage mechanism

To understand the atomic-scale mechanism of the irradiated microstructural features observed in experiments, MD simulations are performed to capture the fine-scale dynamic evolution of irradiation-induced defects. The atomic model of the FeCrNi MEA is shown in Fig. 11a. The elemental distribution of the initial single-crystal MEA is uniform, and the lattice structure is a pure fcc phase at 300 K. Once the cascade collision begins, the PKA first impacts the nearby atoms and results in the simultaneous creation of the same number of vacancies and interstitial atoms, i.e., the Frenkel pairs (Fig. 11b, 12a, and 12d). The interatomic impaction occurs in a local cascade region, and causes the temperature increase and structure disorder in the region (Fig. 11b). During the cascade-collision process, the number of FPs quickly increases (Fig. 12a and 12d), and the cascade region grows (10 ps in Fig. 11b). After the cascade reaction reaches the thermal peak state (20

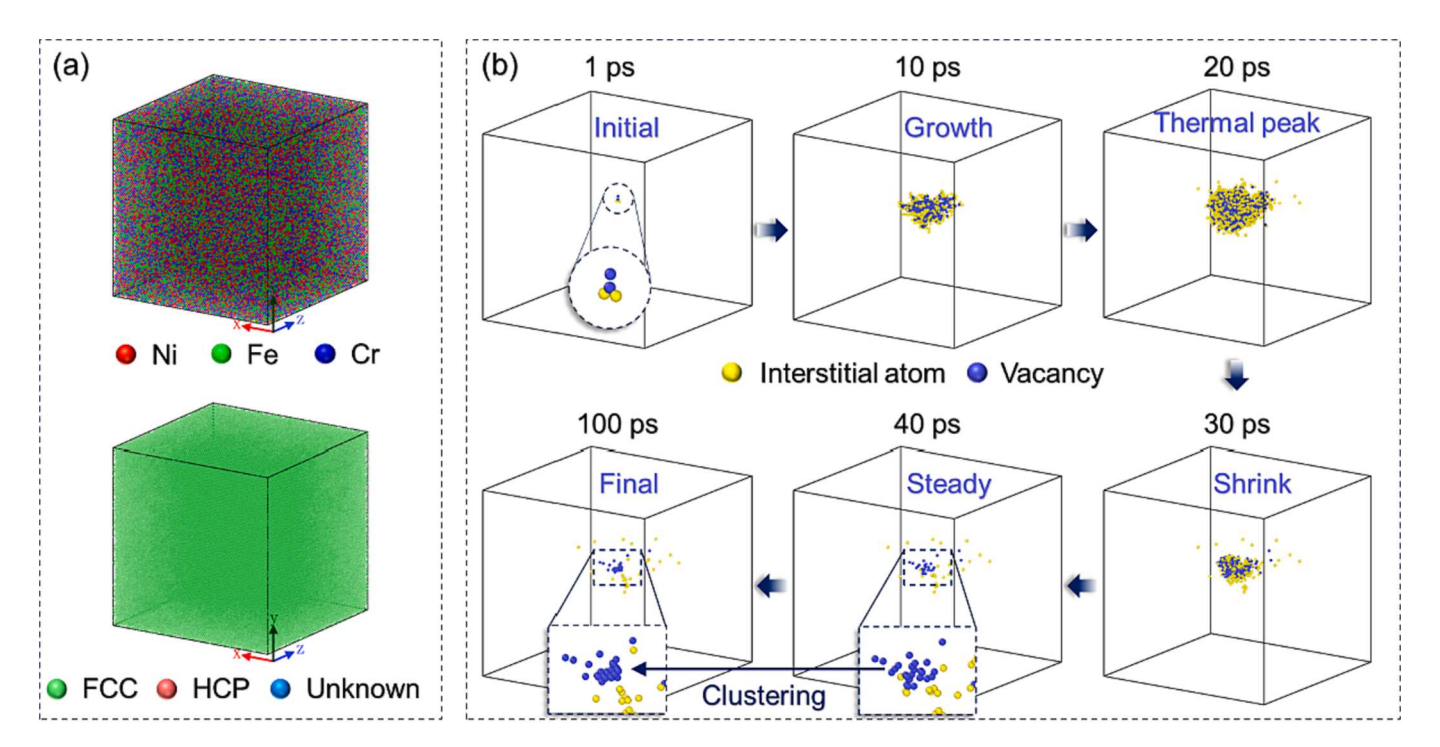


Fig. 11. (a) Atomic model of the FeCrNi MEA, and the lattice structure is analyzed, using the CNA algorithm attached in the OVITO software; (b) representative Frenkel Pairs (FPs) evolution during collision-cascade simulations with 10 KeV PKA.

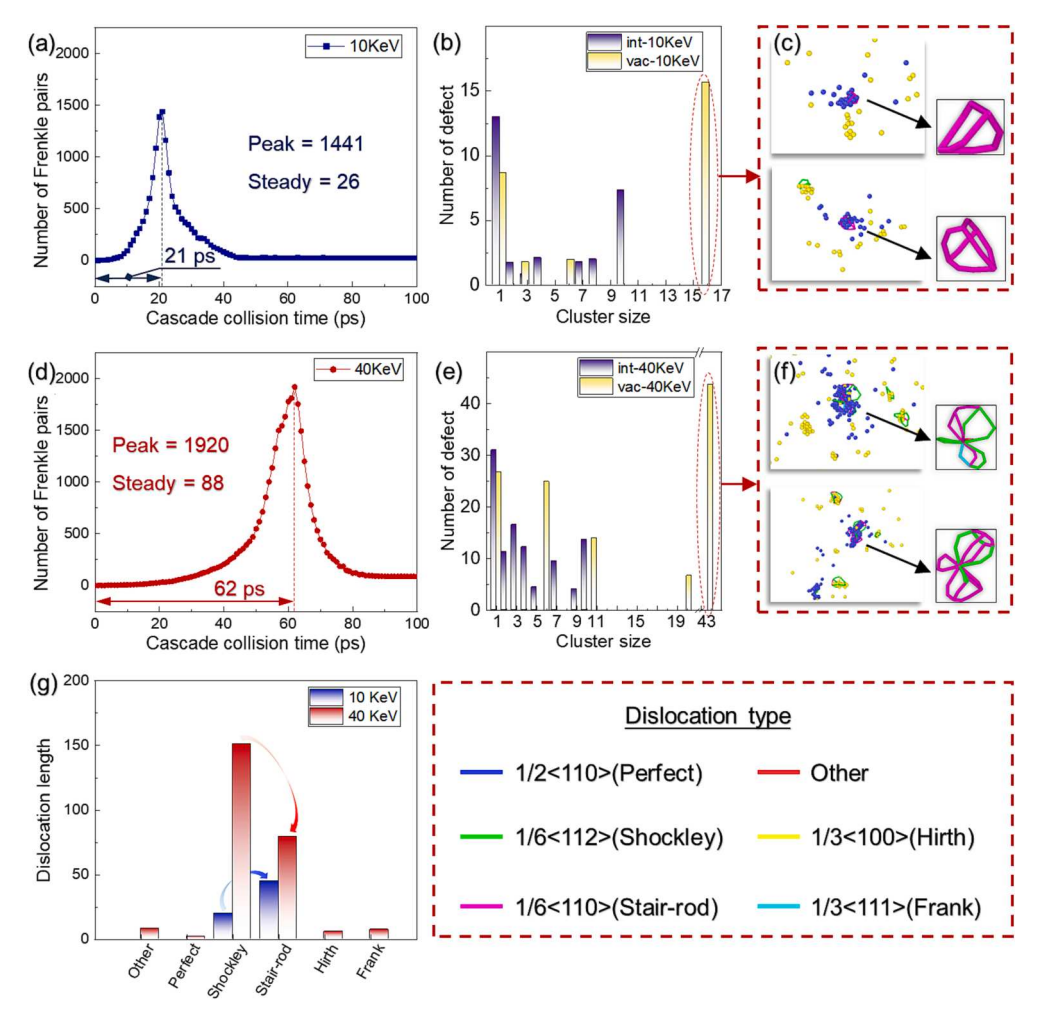


Fig. 12. (a, d) Evolution of the number of FPs during the cascade-collision simulation with 10 KeV and 40 KeV PKAs; (b, e) cluster-size distribution at the final state of the cascade-collision simulation with 10 KeV and 40 KeV PKAs; (c, f) representative atomic details of the final defect clusters and dislocation details of the largest vacancy clusters; (g) the length of different types of dislocation lines at the final state of the cascade-collision simulation. The dislocation is analyzed, using the DXA algorithm in OVITO software.

ps), the cascade region quickly shrinks (30 ps) and arrives at the steady stage (40 ps). The number of FPs is almost unchanged after the steady stage (Fig. 12a and 12d), but some surviving defects will spontaneously cluster together in the subsequent relaxation. Because the vacancy has a relatively low mobility compared to the interstitial atoms, most surviving vacancies stay at the center of the cascade region (Fig. 11b). It can be seen that most originally separately vacancies are more likely to aggregate into large vacancy clusters (100 ps). These large-size defect clusters are the major part to be detected in experiments and are the main reason for material degradation.

The distribution of defect clusters in the final stage of cascade collision is shown in Fig. 12b and 12e. The size of vacancy clusters is larger than that of the interstitial clusters, attributed to the low mobility of vacancies in alloys. The size of defect clusters for the high-energy (40 KeV PKA) cascade collision is also larger than that for the low-energy (10 KeV PKA) cascade collision. These results are consistent with the cascade-collision simulations in the previous literature [11,44]. Interestingly, the large vacancy cluster in the FeCrNi MEA is easy to collapse into the SFT composed with stair-rod dislocations (Fig. 12c and 12f). For the high-energy cascade, the SFT will transfer to complicated dislocation nets due to complicate dislocation reactions (Fig. 12f). Since the vacancy clusters have transformed to SFTs, the formation of large vacancy clusters will be suppressed after irradiation. That provides an explanation for the absence of voids formation in the irradiated FeCrNi MEA (Fig. 6). When a great number of vacancies are consumed for the

production of SFTs, only a small number of vacancies can diffuse. In this case, the segregation and precipitation are suppressed. This trend is also supported by the stable phase structure and the presence of relatively small Au clusters in Fig. 6.

By analyzing the dislocation lengths of different types of dislocations in the final stage of cascade collision, it can be seen that the high-energy cascade triggers more types of dislocations (Fig. 12g). For the lowenergy cascade collision, only the Shockley and Stair-rod dislocations are detected, and the Stair-rod dislocation is the domination. However, for the high-energy cascade, six types of dislocations are observed, and the Shockley dislocations become domination. Note that the slip of a Shockley dislocation is very easy, compared with other dislocations, and the Stair-rod dislocation is always unmovable [45,46]. Therefore, the high-density Shockley dislocations and abundant dislocation types provide a good foundation for the high-frequency dislocation reactions, as well as the interaction between dislocations and irradiation-induced point defects. These results agree well with the high-density dislocations observed in Fig. 6, implying the important role of irradiationinduced Shockley dislocations on affecting the final dislocation networks in the high-fluence irradiated FeCrNi MEA. Because the large-size vacancy clusters are easily to transform into Shockley dislocations under high-energy cascades, it's logical to deduce that the size and distribution of vacancy clusters play a key role on affecting dislocation distributions and dominated dislocation types. In the M/HEAs, the sluggish diffusion effect and unique interstitial atoms movement will effectively suppress the vacancy clustering [11,30,40]. That is beneficial for the dispersed distribution of vacancy clusters and the subsequent uniformly distributed dislocations in irradiated samples.

The high-fraction Shockley dislocations at high-energy irradiation, in combination with the absence of detectable voids and small Au clusters, are important reasons for the insignificant hardening after irradiation. On one hand, extensive moveable Shockley dislocations are easy to be activated, which is helpful for relieving the local stress and contributing to the softening effect of materials. On the other hand, the obstacles for dislocations are less, which are beneficial for the dislocation movement. In all, the atomic-scale evolution of vacancy clusters plays an essential role for the microstructural features of the FeCrNi MEA after irradiation, and finally results in the slight hardening effect under high-fluence ion irradiation.

4. Conclusions

To summarize, a cobalt-free FeCrNi MEA was fabricated via the P/M method, and the irradiation response and damage mechanism of the FeCrNi MEA under high-fluence ion irradiation were investigated. The main conclusion can be listed as follows:

- (1) The FeCrNi MEA exhibits a high-irradiation structure and phase stability and can still maintain a single-phase fcc structure without amorphization even under high-fluence ion irradiation.
- (2) Irradiation-induced dislocations and defect clusters are the primary microstructural feature in the irradiated FeCrNi MEA. At a high irradiation fluence, limited elemental segregation near grain boundaries and fine Au clusters can be found. However, void formation and phase instability are absent in any irradiation condition.
- (3) The MD simulations reveal that the large-size vacancy cluster is easy to transform to the SFT in the FeCrNi MEA, resulting in the absence of void formation in irradiated samples. In addition, high-fraction moveable Shockley dislocations will be activated by the high-energy cascade collision, which are beneficial for weakening the hardening effect under high-fluence irradiation.
- (4) Slight irradiation hardness increases are revealed by nanoindentation tests, and the irradiation hardening is mainly due to the increased lattice strain as well as the irradiation-induced dislocations, and defect clusters acted as barriers to hinder the dislocation slip during the nanoindentation tests.

5. Originality statement

The authors declared that they have no conflicts of interest to this work. We declare that we do not have any commercial or associative interest that represents a conflict of interest in connection with the work submitted.

CRediT authorship contribution statement

Ao Fu: Writing – original draft, Methodology, Investigation, Formal analysis. Bin Liu: Supervision, Project administration, Funding acquisition. Fusheng Tan: Writing – review & editing, Resources. Yuankui Cao: Methodology, Investigation. Jia Li: Formal analysis, Data curation, Conceptualization. Bo Liu: Resources, Conceptualization. Qihong Fang: Formal analysis, Data curation. Peter K. Liaw: Writing – review & editing, Formal analysis. Yong Liu: Supervision, Conceptualization.

Declaration of competing interest

The authors declare that they have no known competing financial interests or personal relationships that could have appeared to influence the work reported in this paper.

Data availability

No data was used for the research described in the article.

Acknowledgements

This study was financially supported by the National Natural Science Foundation of China (52020105013), Natural Science Foundation of Hunan Province (2022JJ20001), and Natural Science Foundation of Hubei Province (2022CFB894). Peter K. Liaw very much appreciates the support the supports from the National Science Foundation (DMR 1611180, 1809640, and 2226508) with program directors, Drs. J. Yang, G. Shiflet, and D. Farkas. The Advanced Research Center at Central South University is also sincerely appreciated for TEM technical support.

References

- R. Hu, S. Jin, G. Sha, Application of atom probe tomography in understanding high entropy alloys: 3D local chemical compositions in atomic scale analysis, Prog. Mater. Sci. 123 (2022) 100854.
- [2] S. Xia, M.C. Gao, T. Yang, P.K. Liaw, Y. Zhang, Phase stability and microstructures of high entropy alloys ion irradiated to high doses, J. Nucl. Mater. 480 (2016) 100–108.
- [3] T. Allen, J. Busby, M. Meyer, D. Petti, Materials challenges for nuclear systems, Mater. Today 13 (2010) 14–23.
- [4] K.L. Murty, I. Charit, Structural materials for Gen-IV nuclear reactors: challenges and opportunities, J. Nucl. Mater. 383 (2008) 189–195.
- [5] T.F. Yang, W. Guo, J.D. Poplawsky, D.Y. Li, L. Wang, Y. Li, W.Y. Hu, M.L. Crespillo, Z.F. Yan, Y. Zhang, Y.G. Wang, S.J. Zinkle, Structural damage and phase stability of Al_{0.3}CoCrFeNi high entropy alloy under high temperature ion irradiation, Acta Mater. 188 (2020) 1–15.
- [6] R. Florez, M.L. Crespillo, X. He, T.A. White, G. Hilmas, W. Fahrenholtz, J. Graham, The irradiation response of ZrC ceramics under 10 MeV Au3+ ion irradiation at 800 °C, J. Eur. Ceram. Soc. 40 (2020) 1791–1800.
- [7] F. Wang, X.L. Yan, T.Y. Wang, Y.Q. Wu, L. Shao, M. Nastasi, Y.F. Lu, B. Cui, Irradiation damage in (Zr0.25Ta0.25Nb0.25Ti0.25)C high-entropy carbide ceramics, Acta Mater. 195 (2020) 739–749.
- [8] M. Sadeghilaridjani, A. Ayyagari, S. Muskeri, V. Hasannaeimi, R. Salloom, W. Y. Chen, S. Mukherjee, Ion irradiation response and mechanical behavior of reduced activity high entropy alloy, J. Nucl. Mater. 529 (2020) 151955.
- [9] C.Y. Lu, T.N. Yang, K. Jin, G. Velisa, P.Y. Xiu, M. Song, Q. Peng, F. Gao, Y. W. Zhang, H.B. Bei, W.J. Weber, L.M. Wang, Enhanced void swelling in NiCoFeCrPd high-entropy alloy by indentation-induced dislocations, Mater. Res. Lett. 6 (2018) 584-591.
- [10] A. Fu, B. Liu, W.J. Lu, B. Liu, J. Li, Q.H. Fang, Z.M. Li, Y. Liu, A novel supersaturated medium entropy alloy with superior tensile properties and corrosion resistance, Scr. Mater. 186 (2020) 381–386.
- [11] Y. Lin, T. Yang, L. Lang, C. Shan, H. Deng, W. Hu, F. Gao, Enhanced radiation tolerance of the Ni-Co-Cr-Fe high-entropy alloy as revealed from primary damage, Acta Mater. 196 (2020) 133–143.
- [12] A. Fu, Y.K. Cao, Z.H. Xie, J. Wang, B. Liu, Microstructure and mechanical properties of Al-Fe-Co-Cr-Ni high entropy alloy fabricated via powder extrusion, J. Alloys Compd. 943 (2023) 169052.
- [13] J. Li, Y. Chen, Q. He, X. Xu, H. Wang, C. Jiang, B. Liu, Q. Fang, Y. Liu, Y. Yang, P. K. Liaw, C.T. Liu, Heterogeneous lattice strain strengthening in severely distorted crystalline solids, Proc. Natl. Acad. Sci. 119 (2022) e2200607119.
- [14] G. Laplanche, A. Kostka, C. Reinhart, J. Hunfeld, G. Eggeler, E.P. George, Reasons for the superior mechanical properties of medium-entropy CrCoNi compared to high-entropy CrMnFeCoNi, Acta Mater. 128 (2017) 292–303.
- [15] A. Fu, B. Liu, Z. Li, B. Wang, Y. Cao, Y. Liu, Dynamic deformation behavior of a FeCrNi medium entropy alloy, J. Mater. Sci. Technol. 100 (2022) 120–128.
- [16] Y. Chen, S. Wang, H. Feng, W. Li, B. Liu, J. Li, Y. Liu, P.K. Liaw, Q. Fang, Irradiation hardening behavior of high entropy alloys using random field theory informed discrete dislocation dynamics simulation, Int. J. Plast. 162 (2023) 103497.
- [17] X. Wang, C.M. Barr, K. Jin, H.B. Bei, K. Hattar, W.J. Weber, Y.W. Zhang, K.L. More, Defect evolution in Ni and NiCoCr by in situ 2.8 MeV Au irradiation, J. Nucl. Mater. 523 (2019) 502–509.
- [18] C. Li, X. Hu, T. Yang, N.K. Kumar, B.D. Wirth, S.J. Zinkle, Neutron irradiation response of a Co-free high entropy alloy, J. Nucl. Mater. 527 (2019) 151838.
- [19] V. Voyevodin, S. Karpov, G. Tolstolutskaya, M. Tikhonovsky, A. Velikodnyi, I. Kopanets, G. Tolmachova, A. Kalchenko, R. Vasilenko, I. Kolodiy, Effect of irradiation on microstructure and hardening of Cr-Fe-Ni-Mn high-entropy alloy and its strengthened version, Phil. Mag. 100 (2020) 822–836.
- [20] A. Fu, B. Liu, B. Liu, Y.K. Cao, J. Wang, T. Liao, J. Li, Q.H. Fang, P.K. Liaw, Y. Liu, A novel cobalt-free oxide dispersion strengthened medium-entropy alloy with outstanding mechanical properties and irradiation resistance, J. Mater. Sci. Technol. 152 (2023) 190–200.
- [21] W.D. Nix, H. Gao, Indentation size effects in crystalline materials: a law for strain gradient plasticity, J. Mech. Phys. Solids 46 (1998) 411–425.
- [22] S. Plimpton, Fast parallel algorithms for short-range molecular dynamics, J. Comput. Phys. 117 (1995) 1–19.

- [23] A. Stukowski, Visualization and analysis of atomistic simulation data with OVITOthe Open Visualization Tool, Model. Simul. Mater. Sci. Eng. 18 (2010) 015012.
- [24] F.S. Tan, J. Li, H. Feng, Q.H. Fang, C. Jiang, Y. Liu, P.K. Liaw, Entropy-induced transition on grain-boundary migration in multi-principal element alloys, Scr. Mater. 194 (2021) 113668.
- [25] J. Li, H.T. Chen, Q.H. Fang, C. Jiang, Y. Liu, P.K. Liaw, Unraveling the dislocationprecipitate interactions in high-entropy alloys, Int. J. Plast. 133 (2020) 102819.
- [26] L.K. Béland, A. Tamm, S. Mu, G.D. Samolyuk, Y.N. Osetsky, A. Aabloo, M. Klintenberg, A. Caro, R.E. Stoller, Accurate classical short-range forces for the study of collision cascades in Fe-Ni-Cr, Comput. Phys. Commun. 219 (2017) 11–19.
- [27] L. Tang, F. Jiang, J. Wróbel, B. Liu, S. Kabra, R. Duan, J. Luan, Z. Jiao, M. Attallah, D. Nguyen-Manh, In situ neutron diffraction unravels deformation mechanisms of a strong and ductile FeCrNi medium entropy alloy, J. Mater. Sci. Technol. 116 (2022) 103–120.
- [28] M. Schneider, G. Laplanche, Effects of temperature on mechanical properties and deformation mechanisms of the equiatomic CrFeNi medium-entropy alloy, Acta Mater. 204 (2021) 116470.
- [29] T. Yang, S. Xia, S. Liu, C. Wang, S. Liu, Y. Fang, Y. Zhang, J. Xue, S. Yan, Y. Wang, Precipitation behavior of Al_xCoCrFeNi high entropy alloys under ion irradiation, Sci. Rep. 6 (2016) 1–8.
- [30] N.A.P.K. Kumar, C. Li, K.J. Leonard, H. Bei, S.J. Zinkle, Microstructural stability and mechanical behavior of FeNiMnCr high entropy alloy under ion irradiation, Acta Mater. 113 (2016) 230–244.
- [31] T. Yang, S. Xia, W. Guo, R. Hu, J.D. Poplawsky, G. Sha, Y. Fang, Z. Yan, C. Wang, C. Li, Effects of temperature on the irradiation responses of Al_{0.1}CoCrFeNi high entropy alloy, Scr. Mater. 144 (2018) 31–35.
- [32] P.P. Cao, H. Wang, J.Y. He, C. Xu, S.H. Jiang, J.L. Du, X.Z. Cao, E.G. Fu, Z.P. Lu, Effects of nanosized precipitates on irradiation behavior of CoCrFeNi high entropy alloys, J. Alloys Compd. 859 (2021) 158291.
- [33] Y. Lu, H. Huang, X. Gao, C. Ren, J. Gao, H. Zhang, S. Zheng, Q. Jin, Y. Zhao, C. Lu, A promising new class of irradiation tolerant materials: Ti₂ZrHfV_{0.5}Mo_{0.2} highentropy alloy, J. Mater. Sci. Technol. 35 (2019) 369–373.
- [34] Z.J. Wang, C.T. Liu, P. Dou, Thermodynamics of vacancies and clusters in highentropy alloys, Phys. Rev. Mater. 1 (2017) 043601.
- [35] W.Y. Chen, J.D. Poplawsky, Y. Chen, W. Guo, J.W. Yeh, Irradiation-induced segregation at dislocation loops in CoCrFeMnNi high entropy alloy, Materialia 14 (2020) 100951.

- [36] C. Lu, T. Yang, K. Jin, N. Gao, P. Xiu, Y. Zhang, F. Gao, H. Bei, W.J. Weber, K. Sun, Y. Dong, L. Wang, Radiation-induced segregation on defect clusters in single-phase concentrated solid-solution alloys, Acta Mater. 127 (2017) 98–107.
- [37] A. Etienne, B. Radiguet, N.J. Cunningham, G.R. Odette, R. Valiev, P. Pareige, Comparison of radiation-induced segregation in ultrafine-grained and conventional 316 austenitic stainless steels, Ultramicroscopy 111 (2011) 659–663.
- [38] G.S. Was, J.P. Wharry, B. Frisbie, B.D. Wirth, D. Morgan, J.D. Tucker, T.R. Allen, Assessment of radiation-induced segregation mechanisms in austenitic and ferriticmartensitic alloys, J. Nucl. Mater. 411 (2011) 41–50.
- [39] T.R. Anthony, Solute segregation in vacancy gradients generated by sintering and temperature changes, Acta Metall. 17 (1969) 603–609.
- [40] C. Lu, L. Niu, N. Chen, K. Jin, T. Yang, P. Xiu, Y. Zhang, F. Gao, H. Bei, S. Shi, M.-R. He, I.M. Robertson, W.J. Weber, L. Wang, Enhancing radiation tolerance by controlling defect mobility and migration pathways in multicomponent single-phase alloys, Nat. Commun. 7 (2016) 13564.
- [41] F. Tuomisto, I. Makkonen, J. Heikinheimo, F. Granberg, F. Djurabekova, K. Nordlund, G. Velisa, H. Bei, H. Xue, W.J. Weber, Y. Zhang, Segregation of Ni at early stages of radiation damage in NiCoFeCr solid solution alloys, Acta Mater. 196 (2020) 44–51.
- [42] M.A. Tunes, G. Greaves, H. Bei, P.D. Edmondson, Y. Zhang, S.E. Donnelly, C. G. Schön, Comparative irradiation response of an austenitic stainless steel with its high-entropy alloy counterpart, Intermetallics 132 (2021) 107130.
- [43] S.K. Shen, F.D. Chen, X.B. Tang, J.W. Lin, G.J. Ge, J. Liu, Effects of carbon doping on irradiation resistance of Fe₃₈Mn₄₀Ni₁₁Al₄Cr₇ high entropy alloys, J. Nuc. Mater. 540 (2020) 152380.
- [44] S. Zhao, Y. Xiong, S. Ma, J. Zhang, B. Xu, J.-J. Kai, Defect accumulation and evolution in refractory multi-principal element alloys, Acta Mater. 219 (2021) 117233
- [45] C. Dong, X. Lu, P. Yang, X. Guo, J. Ren, H. Xue, J. Li, F. Tang, H. Li, Y. Ding, P. La, Effects of crystallographic orientation, temperature and void on tensile mechanical properties of Ni-Co single crystal nanopillars, J. Alloys Compd. 870 (2021) 159476.
- [46] Z.X. Wu, Y.W. Zhang, D.J. Srolovitz, Dislocation-twin interaction mechanisms for ultrahigh strength and ductility in nanotwinned metals, Acta Mater. 57 (2009) 4508–4518